ARMA 17-0679

Mixed-mode dynamic crack propagation in rocks with contact-separation mode transitions

Abedi, R.
Department of Mechanical, Aerospace & Biomedical Engineering, The University of Tennessee Space Institute, TN, USA

Haber, R.B.
Mechanical Science and Engineering, University of Illinois at Urbana-Champaign, Urbana, IL, USA

Elbanna, A.
Civil and Environmental Engineering, University of Illinois at Urbana-Champaign, Urbana, IL, USA

This paper was prepared for presentation at the 51st US Rock Mechanics / Geomechanics Symposium held in San Francisco, California, USA, 25-28 June 2017.

ABSTRACT: We propose an interfacial contact/damage model for simulating dynamic fracture in rocks. An interfacial damage parameter, D, models the evolution of damage on fracture interfaces, while relative contact and contact–stick fractions model contact–separation and stick–slip transitions. The damage rate is determined by an effective stress, written as a scalar function of the normal and tangential components of the Riemann traction solution for assumed bonded conditions. We propose alternative definitions of the effective stress that generate failure criteria that resemble the Tresca and Mohr–Coulomb criteria for compressive stress states, and we compare their compressive strengths and fracture angles under a compressive loading. We adopt a stochastic Weibull model for crack-nucleation in which cracks nucleate at points where the effective stress exceeds the probabilistic fracture strength. We implement the nucleation model with an h-adaptive asynchronous spacetime discontinuous Galerkin (aSDG) method that captures accurately the complex fracture patterns that arise under dynamic loading conditions. Numerical examples illustrate the effects on fracture response of varying the stochastic nucleation parameters and the alternative definitions of the effective stress.

Acknowledgments: The authors gratefully acknowledge partial support for this work via the U.S. National Science Foundation (NSF), CMMI - Mechanics of Materials and Structures (MoMS) program grant number 1538332.

1 INTRODUCTION

Understanding the stress states that cause rock failure is critical to the reliable analysis and safe design of structures in rocks. In situ rock is typically subjected to compressive stress fields, and experimental observations indicate that the compressive strength of rock increases with increasing confining pressure. Failure occurs by shearing along planes oriented at a rock-type-specific angle, θ, defined relative to the direction of maximum compressive stress [1]. *Failure criteria* describe the variation of compressive strength with confining pressure and, in general, the stress states at which rock fails.

A number of failure criteria have been proposed in rock mechanics. The *Tresca criterion* assumes that a material fails on planes with maximum shear stress. While it is sometimes used for failure analysis of rock [2], the Tresca criterion is more appropriate for ductile materials as its corresponding shear strength is independent of the confinement pressure. The *Mohr–Coulomb* (MC) failure criterion depends linearly on the normal and shear stress components. This implies a linear relation between confinement pressure and compressive strength. However, this straight-line relation does not always fit experimental data [3], and the extension of the linear relation into the tensile loading regime generally over-predicts the tensile strength of rock. Experiments show that the rates of increase of the shear and compressive strengths decrease as confinement pressure increases. In fact, beyond a certain confinement pressure, rock reaches a *critical state* at which the shear strength no longer increases, similar to the constant shear strength of the Tresca model [4]. Beyond the limitations associated with linearity of the Mohr–Coulomb model, various studies demonstrate that fully three-dimensional failure criteria are required to capture the influence of the intermediate principal stress [5–8]. However, due to its simplicity and the challenges involved in calibrating the more advanced models, the Mohr-Coulomb model is still the most popular and widely used-failure criterion for rock.

In this work, we propose an interfacial damage model for fracture and slip in rock under compressive stress states that combines dynamically-consistent Riemann solutions

for various contact modes across contact/fracture interfaces. A scalar *effective stress*, drives damage evolution on fracture interfaces. We propose two alternative definitions of the effective stress in 3.2 that match, respectively, the Tresca model and the Mohr–Coulomb model under compressive loading.

We use an h-adaptive *asynchronous spacetime Discontinuous Galerkin* (aSDG) method [9, 10] and advanced spacetime adaptive operations [11, 12] to track exactly the incremental crack-propagation directions predicted by our failure criteria. A stochastic model for fracture strength that models the effects of microscopic flaws [11, 13] governs when and where we nucleate new cracks. We compare the alternative effective stress stress models in terms of their compressive strengths, fracture angles θ, and the fracture patterns they predict in combination with the aSDG method. We present results for problems without pre-existing cracks and study the influence of the stochastic model parameters on fracture patterns in §5. These results demonstrate the importance of stochastic models in fracture simulation and their effectiveness when implemented with the proposed effective stress models in the aSDG solver.

2 A RATE-DEPENDENT INTERFACIAL DAMAGE MODEL

Material degradation in continuum models can be represented as a bulk material process, or in the case of fracture, by the nucleation and propagation of sharp-interface cracks. Cohesive models, the most popular representation in sharp-interface crack models, use a *traction–separation relation* (TSR) to model the tractions acting across a fracture as nonlinear functions of the displacement jump across the interface. However, enforcement of the impenetrability condition and modeling frictional contact during crack closure are challenging with TSRs.

In lieu of a traditional cohesive model, we present an interfacial damage model, first introduced in [11], that represents dynamic processes of debonding and contact on *fracture interfaces*, *i.e.,* surfaces where a fracture already exists or may develop in the future. We use a scalar damage parameter, D, to interpolate between intact ($D = 0$) and failed ($D = 1$) states. Rather than degrade an interfacial stiffness, we interpolate between dynamically consistent Riemann solutions for fully bonded (intact) and fully debonded (failed) conditions to determine the jump conditions across fracture interfaces. The Riemann solutions for fully debonded conditions include all subcases for separation, contact–stick, and contact–slip modes, including frictional effects, as described in [14]. Enforcement of these Riemann solutions ensures satisfaction of the impenetrability condition for crack closure without resorting to penalty or other constraint methods.

We describe Riemann solutions for fully bonded conditions and for the various debonded contact and separation modes in §2.1, and in §2.2, their combination in the definition of dynamically consistent macroscopic target values across a fracture surface. We present the effective stress definitions and the damage evolution equation In §3.

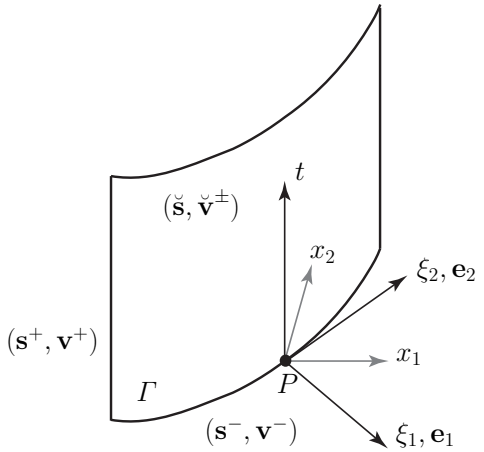

Figure 1: Local coordinate frame at an arbitrary spacetime location P on a spacetime fracture surface Γ for a problem in two spatial dimensions.

2.1 Riemann solutions for the various contact modes

For completeness, this section provides a short overview of different Riemann contact solutions from [14]. The solutions for individual contact modes are obtained by solving local Riemann problems at a contact interface. A local coordinate frame at an arbitrary spacetime location P on contact interface Γ is illustrated in fig. 1. The local coordinates are (ξ_1, ξ_2, t), and the frame is oriented such that the ξ_1-direction aligns with the spatial normal vector on Γ.

The quantities from opposite sides of Γ, decorated with superscripts $+$ and $-$, define the initial data for the Riemann problem. Distinct velocity traces, $\mathbf{v}^{\pm}$, and tractions, $\mathbf{s}^{\pm}$, defined by $\mathbf{s} = \boldsymbol{\sigma} \cdot \mathbf{n}$ in which the same spatial normal vector, $\mathbf{n}$, is used to compute $\mathbf{s}^+$ and $\mathbf{s}^-$ from the distinct traces of the stress tensor field on the interface, $\boldsymbol{\sigma}^{\pm}$. The Riemann values at a given point P on the interface include components of the traction vector acting on the interface and traces of the velocity components from each side of the interface. We denote these by $(\breve{\mathbf{s}}, \breve{\mathbf{v}}^{\pm})$, as shown in the figure. Balance of linear momentum requires equality between the traction vectors obtained from the stress fields on opposite sides of the interface. That is, $\breve{\mathbf{s}}^+ = \breve{\mathbf{s}}^- := \breve{\mathbf{s}}$.

The kinematic compatibility conditions on the interface depend on whether the material interface is intact (perfectly bonded), or in the debonded case, on the specific contact mode. The velocity is continuous across Γ for the bonded and contact–stick cases. For the contact–slip case, the impenetrability condition requires continuity of the normal velocity component, $\breve{v}_1^+ = \breve{v}_1^-$, while possible slip admits discontinuities in the tangential velocity components. In separation mode, all components of $\breve{\mathbf{v}}^+$ and $\breve{\mathbf{v}}^-$ may be discontinuous.

The Riemann solutions are obtained by preserving the

characteristic values of the elastodynamic problem across the fracture surface while enforcing the aforementioned compatibility conditions. For an isotropic material in linear elastodynamics, the spacetime characteristic trajectories in all directions are determined by the dilatational and shear wave speeds, $c_d^{\pm}$ and $c_s^{\pm}$, in which

$$c_{\mathrm{d}} = \sqrt{\frac{\lambda + 2\mu}{\rho}}, \qquad c_{\mathrm{s}} = \sqrt{\frac{\mu}{\rho}}. \tag{1}$$

where ρ is mass density and λ, μ are Lamé parameters.

The characteristic values depend on impedance values,

$$Z^{i\pm} := \begin{cases} (c_d \rho)^{\pm} & i = 1 \\ (c_s \rho)^{\pm} & i = 2, 3 \end{cases} \tag{2}$$

in which the index i corresponds to spatial directions in the local frame shown in fig. 1; *cf.* [14]. The Riemann solutions for contact–stick and bonded modes, decorated with subscripts ST and B respectively, are

$$\breve{s}^i_{\mathrm{B}} = \breve{s}^i_{\mathrm{ST}} = \breve{s}^i = \frac{s^{i+} Z^{i-} + s^{i-} Z^{i+}}{Z^{i-} + Z^{i+}} + \frac{Z^{i-} Z^{i+}}{Z^{i-} + Z^{i+}} (v_i^+ - v_i^-) \tag{3a}$$

$$\breve{v}^{\mathrm{B}}_i = \breve{v}^{\mathrm{ST}}_i = \breve{v}_i = \frac{s^{i-} - s^{i+}}{Z^{i-} + Z^{i+}} + \frac{v_i^+ Z^{i+} + v_i^- Z^{i-}}{Z^{i-} + Z^{i+}} \tag{3b}$$

in which no summation is implied for repeated indices i.

In separation mode, $\breve{\mathbf{v}}^+$ and $\breve{\mathbf{v}}^-$ are independent. The Riemann tractions are set equal to a value, $\mathbf{S}$, determined by a particular fracture model or a prescribed crack-surface loading. For example, $\mathbf{S}$ can be the traction induced by a prescribed hydraulic pressure in hydraulic fracturing applications, or we can set $\mathbf{S} = \mathbf{0}$ to model unloaded fracture surfaces, as in [14]. The Riemann solutions for the separation case, decorated by S, are then obtained by preserving the characteristic values on each side of the interface,

$$\breve{s}^i_{\mathrm{S}} = \breve{s}^i = S^i \tag{4a}$$

$$\breve{v}^{\mathrm{S}\pm}_i = \breve{v}^{\pm}_i = v^{\pm}_i \pm \frac{S^i - s^{i\pm}}{Z^{i\pm}} \tag{4b}$$

For the transition between contact–stick and contact–slip modes we use the Mohr–Coulomb friction law. The magnitude of tangential traction, for bonded Riemann solutions, *cf.* (3a), is defined as,

$$\breve{\tau}_{\mathrm{B}} := \sqrt{\left(\breve{s}^2_{\mathrm{B}}\right)^2 + \left(\breve{s}^3_{\mathrm{B}}\right)^2} \tag{5}$$

for $d = 3$. For two spatial dimensions ($d = 2$), $\breve{\tau}_{\mathrm{B}} = |\breve{s}^2_{\mathrm{B}}|$. When the normal displacement jump and the bonded Riemann value for the normal traction, $\breve{s}^1_{\mathrm{B}}$, indicate contact conditions, the interface enters slip mode if $\breve{\tau}_{\mathrm{B}}$ satisfies the Coulomb slip condition,

$$|\breve{\tau}_{\mathrm{B}}| > k \left\langle -\breve{s}^1_{\mathrm{B}} \right\rangle_+ \tag{6}$$

in which k is the friction coefficient and $\langle . \rangle_+$ is the positive Macaulay bracket. Under these conditions, the tangential component of the Riemann traction vector aligns with the interfacial slip velocity and its magnitude is given by $k \left\langle -\breve{s}^1_{\mathrm{B}} \right\rangle_+$; *cf.* Fig. 4 as well as a method for handling stick–slip transitions where the slip direction is undefined in [14]. Enforcing the normal components of the bonded Riemann solution and the Mohr–Coulomb friction law for tangential components, we obtain the slip-mode Riemann solutions, indicated by superscripts SL,

$$\breve{s}^i_{\mathrm{SL}} = \breve{s}^i = \begin{cases} \breve{s}^1_{\mathrm{B}} & i = 1 \\ k \left\langle -\breve{s}^1_{\mathrm{B}} \right\rangle_+ \mathbf{e}^i_{\tau} & i = 2, 3 \end{cases} \tag{7a}$$

$$\breve{v}^{\mathrm{SL}\pm}_i = \breve{v}^{\pm}_i = \begin{cases} \breve{s}^{\mathrm{B}}_1 & i = 1 \\ v^{\pm}_i \pm \frac{\breve{s}^i_{\mathrm{SL}} - s^{i\pm}}{Z^{i\pm}} & i = 2, 3 \end{cases} \tag{7b}$$

2.2 Macroscopic target values

We use the damage parameter, D, to interpolate between the *bonded* and *debonded* Riemann solutions on Γ,

$$\mathbf{s}^* := (1 - D)\breve{\mathbf{s}}_B + D\breve{\mathbf{s}}_D \tag{8a}$$

$$\mathbf{v}^{*\pm} := (1 - D)\breve{\mathbf{v}}_B + D\breve{\mathbf{v}}^{\pm}_D \tag{8b}$$

in which subscripts B and D denote Riemann values for bonded and debonded conditions. Thus, D, can be interpreted as the relative fraction of debonded surface in the neighborhood of any location on Γ.

To evaluate the debonded Riemann solution, we must first determine whether contact or separation mode holds for the debonded part. Separation conditions hold when the normal bonded traction $\breve{s}^1_{\mathrm{B}}$ is positive or the normal displacement jump is positive. Otherwise, the interface is in contact mode. Transitions from separation to contact modes are physically non-smooth, so a regularization is introduced to enhance numerical convergence, as explained in [14]. We introduce a regularization parameter for this purpose called the *relative contact fraction*, $\eta \in [0\ 1]$, where $\eta = 1$ indicates full contact mode. Transitions from contact to separation, on the other hand, are physically and mathematically smooth and require no regularization. We apply the Mohr–Coulomb condition (6) to determine whether contact–stick or contact–slip conditions hold on the contact part of the debonded fraction. The binary state *relative stick fraction*, $\gamma \in \{0, 1\}$, indicates which of the two modes hold on the contact part, with $\gamma = 1$ corresponding to contact–stick mode.

In short, $\breve{\mathbf{s}}_D$ and $\breve{\mathbf{v}}^{\pm}_D$ are themselves interpolations of separation solutions (4), bonded/contact–stick solutions (3), and contact–slip (7) solutions. Considering the three relative fractions, D, η, and γ, it is easy to show that $\mathbf{s}^*$ and $\mathbf{v}^{*\pm}$ in (8) can be expressed as linear sums of the Riemann solutions from three distinct response modes, bonded/contact–stick (B), contact–slip (SL), and separation (S):

$$\mathbf{s}^* := a_{\mathrm{B}} \breve{\mathbf{s}}_{\mathrm{B}} + a_{\mathrm{SL}} \breve{\mathbf{s}}_{\mathrm{SL}} + a_{\mathrm{S}} \breve{\mathbf{s}}_{\mathrm{S}} \tag{9a}$$

$$\mathbf{v}^{*\pm} := a_{\mathrm{B}} \breve{\mathbf{v}}_{\mathrm{B}} + a_{\mathrm{SL}} \breve{\mathbf{v}}^{\pm}_{\mathrm{SL}} + a_{\mathrm{S}} \breve{\mathbf{v}}^{\pm}_{\mathrm{S}} \tag{9b}$$

where

$$a_{\mathrm{B}} = 1 - D + D\eta\gamma \tag{10a}$$

$$a_{\mathrm{SL}} = D\eta(1 - \gamma) \tag{10b}$$

$$a_{\mathrm{S}} = D(1 - \eta) \tag{10c}$$

and $a_{\mathrm{B}}, a_{\mathrm{SL}}, a_{\mathrm{S}} \in [0,\ 1]$.

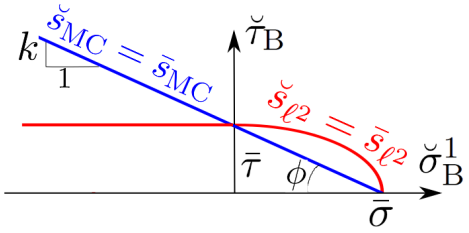

Figure 2: Failure criteria in terms of normal component, $\breve{\sigma}^1_B$, and magnitude of tangential component, $\breve{\tau}_B$, of bonded Riemann tractions for alternative effective stress definitions.

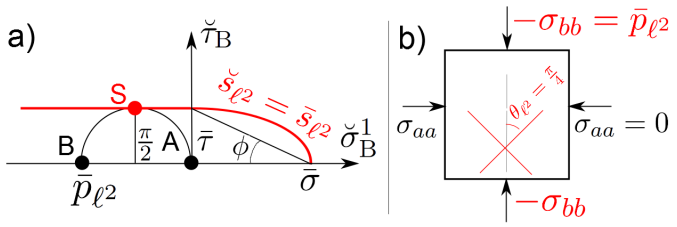

Figure 3: Determination of pressure strength $\bar{p}_{\ell^2}$ and angle θ_{ℓ^2} for the ℓ^2 effective stress model.

3 INTERFACIAL DAMAGE EVOLUTION

This section presents an evolution law for the damage field, D, and introduces alternative definitions for the scalar effective stress that determines the driving force for damage evolution.

3.1 Damage evolution law

Bulk damage models that lack a microscopic length scale may generate non-convergent numerical solutions where damage localizes to layers whose width continues to shrink without limit as the mesh is refined [15,16]. They may also exhibit convergence problems. Similar issues arise in interfacial damage models that lack microscopic length scales. A stabilizing length scale can either be introduced directly in the governing equations or indirectly via a time scale in the damage evolution equations. Examples of the latter type are presented in [17] for bulk damage models and in [16, 18] for interfacial damage models.

Following the model in [19], we adopt the damage evolution equation,

$$\dot{D} = \begin{cases} \frac{1}{\tilde{\tau}}[1 - H(\langle D_t - D\rangle)] & D < 1 \\ 0 & D = 1 \end{cases}, \tag{11}$$

in which $\tilde{\tau}$ is a *relaxation time*, and D_t is a *target damage value*. In general, the function H has unit value at zero and decreases monotonically to 0 at infinity. Following [19], we use $H(x) = \exp(-ax)$, a form that enforces a maximum damage rate of $1/\tilde{\tau}$.

In general, the target damage value D_t depends on the states on both sides of the interface. In this work, we focus on mechanical damage processes and assume that bonded Riemann tractions drive the damage evolution. The justification arises from the fact that we can associate $1-D$ and D with the bonded and debonded microscopic fractions in the neighborhood of a point on Γ. Since the bonded Riemann tractions in (3a) act on the remaining undamaged fraction, the locus of continuing damage, the bonded tractions are the driving force for additional damage. Accordingly, we introduce a scalar *effective stress*, $\breve{s}$, defined as a function of the normal component, $\breve{s}^1_B$ in (3a), and the magnitude of the tangential component, $\breve{\tau}_B$ in (5), of the bonded Riemann traction.[1] That is,

$$\breve{s} := f(\breve{s}^1_B, \breve{\tau}_B), \tag{12}$$

where f is a two-argument scalar function. Alternative choices for f are discussed in §3.2.

We write the target damage value as a function of $\breve{s}$,

$$D_t = \begin{cases} 0 & \breve{s} < \underline{s}, \\ \frac{\breve{s}-\underline{s}}{\bar{s}-\underline{s}} & \underline{s} \le \breve{s} < \bar{s}\,, \\ 1 & \bar{s} \le \breve{s} \end{cases} \tag{13}$$

in which $0 < \underline{s} < \bar{s}$, and $\underline{s}$ and $\bar{s}$ denote, respectively, thresholds for the onset of additional damage evolution and for attainment of the maximum damage rate, $1/\tilde{\tau}$. We refer to $\bar{s}$ as the *fracture strength*. If $\breve{s} < \underline{s}$, we get $D_t = 0$, and (11) delivers $\dot{D} = 0$. We call the ratio, $c_0 := \underline{s}/\bar{s}$ $(0 < c_0 < 1)$, the *brittleness factor* because higher values of c_0 imply a more brittle fracture process.

3.2 Choices for the effective stress

This subsection presents alternative definitions for the effective stress; *cf.* (12). The condition, $\breve{s} = \bar{s}$, defines a *failure criterion* for each case where the maximum target damage value, $D_t = 1$, is attained in (13). If the interfacial loading is strictly tensile, so that $\breve{\tau}_B = 0$, the tensile strength, $\bar{\sigma}$, is the value of $\breve{\sigma}^1_B$ at which $D_t = 1$. Conversely, if the interface is loaded exclusively in shear, so that $\breve{\sigma}^1_B = 0$, the shear strength $\bar{\tau}$ (or *cohesion* in rock mechanics) is defined as the value of $\breve{\tau}_B$ for which $D_t = 1$. Each effective stress definition includes an internal parameter that adjusts the relative weighting of $\breve{\sigma}^1_B$ and $\breve{\tau}_B$. We can adjust these parameters to match both the tensile and shear strengths between the two models.

3.2.1 ℓ^2 effective stress model

The ℓ^2 *model* defines the effective stress as the ℓ^2 norm of $(\langle\breve{\sigma}^1_B\rangle, \beta\breve{\tau}_B)$; *i.e.*,

$$\breve{s}_{\ell^2} := \sqrt{\langle\breve{s}^1_B\rangle^2 + (\beta\breve{\tau}_B)^2} \tag{14}$$

[1] Our use of the term, *effective stress*, should not be confused with its use in rock mechanics, where it commonly refers to the compressive part of the normal traction less the pore pressure.

in which the *shear stress factor*, β, adjusts the influence of the tangential component of the Riemann traction, and the Macaulay brackets, $\langle . \rangle$, ensure that only tensile normal tractions drive damage evolution. From here on, we use subscripts ℓ^2 to label quantities associated with the ℓ^2 effective stress model. This definition of effective stress has been used in the context of cohesive fracture models, *e.g.,* [20], and in interfacial damage models by the authors [11, 12]. As discussed above, we obtain the tensile and shear strengths by setting $\breve{s}_{\ell^2} = \bar{s}$ for pure tensile and shear modes, respectively. This yields,

$$\bar{\sigma}_{\ell^2} = \bar{s}_{\ell^2} \tag{15a}$$

$$\bar{\tau}_{\ell^2} = \frac{\bar{s}_{\ell^2}}{\beta} \tag{15b}$$

that is, $\bar{\sigma}_{\ell^2}/\bar{\tau}_{\ell^2} = 1/\beta$ and $\bar{s}_{\ell^2}$ refers to the tensile strength of the interface. The red curve in fig. 2 shows the failure criterion for the ℓ^2 model. It covers pure tensile and pure shear states as well as mixed-mode and compressive loading.

3.2.2 Mohr–Coulomb effective stress model

The Mohr–Coulomb effective stress takes the form,

$$\breve{s}_{\text{MC}} := \breve{\tau}_{\text{B}} + k\breve{\sigma}^1_{\text{B}} \tag{16}$$

in which a subscript, MC indicates a quantity in the Mohr–Coulomb effective stress model, and k is the friction coefficient introduced in (6), from which the *angle of friction* ϕ is defined as,

$$\phi = \tan^{-1}(k) \tag{17}$$

Equation (16) has a similar form to (6), in that for a debonded interface and $\breve{\sigma}^1_{\text{B}} < 0$, $\breve{s}_{\text{MC}} = 0$ corresponds to the transition between stick and slip modes.

The tensile and shear strengths are again obtained by setting $\breve{s}_{\text{MC}} = \bar{s}$. This yields,

$$\bar{\sigma}_{\text{MC}} = \bar{s}_{\text{MC}}/k \tag{18a}$$

$$\bar{\tau}_{\text{MC}} = \bar{s}_{\text{MC}} \tag{18b}$$

Equation (18b) shows that $\bar{s}_{\text{MC}}$ is the shear strength (cohesion) of the interface.

The blue line in fig. 2 shows the Mohr-Coulomb failure criterion. From (18) we observe that $\bar{\sigma}_{\text{MC}} = \bar{\tau}_{\text{MC}}/k$. That is, the tensile strength is equal to the cohesion divided by the coefficient of friction. In practice, the tensile strength of rock typically ranges from 5% to 10% of cohesion. However, based on realistic values of the friction coefficient, $\bar{\sigma}_{\text{MC}} = \bar{\tau}_{\text{MC}}/k$ predicts much higher values for $\bar{\sigma}_{\text{MC}}$. This discrepancy is due to the assumed linear extension of the Mohr-Coulomb failure criterion for compressive stress states into the tensile regime. In fact, the failure envelope typically intersects the horizontal axis at a much smaller values of $\bar{\sigma}_{\text{MC}}$ than the linear extension predicts.

If we match the tensile and shear strengths of the two models according to (15) and (18), we obtain

$$\left.\begin{aligned} \bar{\sigma} &:= \bar{\sigma}_{\ell^2} = \bar{\sigma}_{\text{MC}} \\ \bar{\tau} &:= \bar{\tau}_{\ell^2} = \bar{\tau}_{\text{MC}} \end{aligned}\right\} \quad \Rightarrow \quad \beta = \frac{1}{k}, \quad \bar{s}_{\text{MC}} = k\bar{s}_{\ell^2} \tag{19}$$

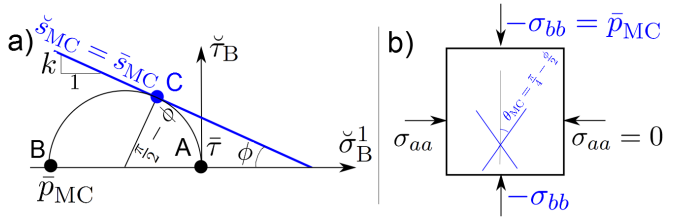

Figure 4: Determination of the compressive strength, $\bar{p}_{\text{MC}}$, and the critical angle, θ_{MC}, in the Mohr–Coulomb effective stress model.

3.2.3 Comparison of the effective stress models

Figure 3a) shows the Mohr's circle for a uniaxial compression loading and the Mohr–Coulomb failure criterion in the $\breve{\sigma}^1_{\text{B}}$ and $\breve{\tau}_{\text{B}}$ plane. As shown in fig. 3b) the points A and B in fig. 3a) correspond to $\sigma_{aa} = 0$ at angle 0 and $\sigma_{aa} = \bar{p}_{\ell^2}$, the compressive strength for the ℓ^2 effective stress model, at angle $\pi/2$, respectively. From the Mohr's circle it is evident that,

$$\bar{p}_{\ell^2} = 2\bar{\tau} = 2k\bar{\sigma} \tag{20a}$$

$$\theta_{\ell^2} = \pm\frac{\pi}{4} \tag{20b}$$

where $\bar{p}_{\ell^2}$, and θ_{ℓ^2}, the angle at which fracture happens, are shown in fig. 3b).

Figure 4 shows the Mohr's circle and failure angle, similar to fig. 3, but for Mohr–Coulomb effective stress. Figure 4a) shows that $\pi/2 - \phi$ is the critical angle at which the Mohr's circle first becomes tangent to the failure criterion line as $\sigma_{bb} \to -\bar{p}_{\text{MC}}$. Combining this result with simple geometric identities, we obtain the compressive strength, $\bar{p}_{\text{MC}}$, and the failure angle, θ_{MC}, for the Mohr–Coulomb effective stress model:

$$\bar{p}_{\text{MC}} = 2\bar{\sigma}k^2\left[1 + \sqrt{1 + \left(\frac{1}{k}\right)^2}\right] \tag{21a}$$

$$\theta_{\text{MC}} = \pm\left(\frac{\pi}{4} - \frac{\phi}{2}\right) \tag{21b}$$

The angle θ_{MC} is shown in fig. 4b). In the ℓ^2 model, the difference $\sigma_{aa} - \sigma_{bb}$ is always $2\bar{\tau}$, even if $\sigma_{aa} < 0$. Whereas with the Mohr–Coulomb model, a larger difference in compressive stress is needed to cause failure as the transverse confinement stress, σ_{aa}, decreases. That is, $\sigma_{aa} - \sigma_{bb}$ increases as σ_{aa} decreases in the Mohr–Coulomb model.

The Mohr–Coulomb effective stress model predicts a larger compressive stress than the ℓ^2 model, mainly due to strengthening of the material under increasing compressive loading; *cf.* (20a), (21a). Figure 5 presents normalized compressive strengths for the two models as a function of the friction coefficient, $k \in [0, 1]$ (in most rock, $k \in [0.2, 0.7]$). The ℓ^2 model delivers $\bar{p}_{\ell^2}/\bar{\tau} = 2$ for all values of of k, while values of $\bar{p}_{\text{MC}}/\bar{\tau}$ in the Mohr–Coulomb model start from 2 at $k = 0$ and grow to $2(1 + \sqrt{2})$ at $k = 1$ where $\bar{p}_{\text{MC}}/\bar{p}_{\ell^2} \approx 2.4$. The fracture angle is always $\pi/4$ in the ℓ^2 model while, as shown in fig. 4b), the

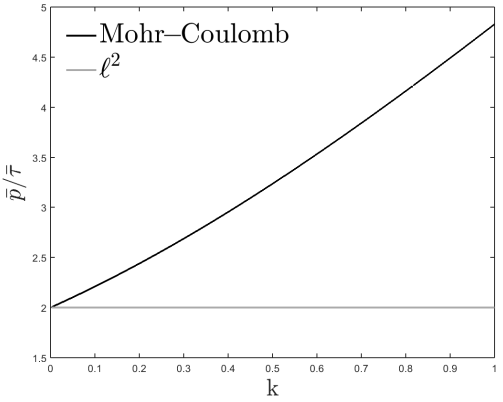

Figure 5: Comparison of compressive strength $\bar{p}$, normalized by shear strength $\bar{\tau}$, of the two effective stress models.

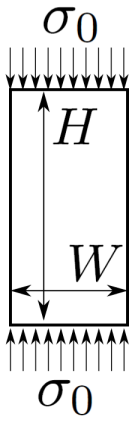

Figure 6: Domain geometry and loading for rectangular-domain fracture problem.

Mohr–Coulomb fracture angle is steeper by $\theta_{\mathrm{MC}}/2$. These observations hold even for nonzero σ_{aa}. In general, the Mohr–Coulomb failure angle moves closer to the direction of the largest compressive load (*i.e.,* σ_{bb} if $\sigma_{bb} < \sigma_{aa}$) as k increases.

4 STOCHASTIC FRACTURE NUCLEATION MODEL AND ADAPTIVE aSDG IMPLEMENTATION

The authors discuss the importance and advantages of using a stochastic model for crack nucleation in [13]. For brevity, we only provide the necessary material needed for explaining numerical results in §5. We base our probabilistic crack nucleation criteria on the Weibull model [21,22], since it models probabilistic fracture strength and size effects in quasi-brittle materials such as rock reasonably well. The *cumulative distribution function* (CDF) for the fracture strength, $\bar{s}$, of a region with given area A is

$$P(\check{s}) = 1 - e^{-\frac{\mathrm{A}}{A_0}\left(\frac{\check{s} - s_{\min}}{s_0}\right)^m} \tag{22}$$

in which A_0 is a reference area such as the area of an experimental rock specimen used to calibrate the Weibull model, s_0 is a strength scale, m is the Weibull modulus, and $s_{\min}$ is a lower bound for the fracture strength; *cf.* (13). Lower values of s_0 imply lower fracture fracture strengths, as do smaller values of A_0. From the discussion above, it is evident that nucleation strength is the same as fracture strength. That is, a crack is nucleated at a position if its corresponding effective stress reaches the fracture strength of the point. The sampled fracture strength is also used for damage evolution on any cracks propagated from the nucleation point through (13).

We use an h-adaptive asynchronous spacetime discontinuous Galerkin (aSDG) method [9,10] to solve the elastodynamics problem in our dynamic simulations of rock fracture. The aSDG method's local and asynchronous solution structure, linear computational complexity, and support for arbitrarily high-order discretizations in both space and time make it ideal for simulating dynamic fracture in rock. We use the aSDG method's powerful spacetime adaptive meshing capabilities to capture the fine details of elastodynamic solutions and to align inter-element boundaries with arbitrary, solution-dependent nucleation sites and crack paths [11,23].

The aSDG method advances the solution in time by solving local patches of elements in spacetime. Each patch includes a small number of elements. For example, for 2D problems there are roughly an average of six tetrahedral elements in a patch, where the vertical axis corresponds to time. The spatial projection of these patches often involves a group of triangles, with total area A, around a vertex V. When sampling a random fracture strength $\bar{s}$ for vertex V, the spatial area of the patch A is used to modulate the Weibull model in (22). The factor A/A_0 in the Weibull CDF models size effect by providing smaller fracture strengths as larger domains (larger A) are considered. For further details on sampling fracture strength values in the aSDG method, please refer to [11,23].

5 NUMERICAL RESULTS

5.1 Rock fracture in compressive mode

5.2 Fracture in a rectangular domain under dynamic compressive loading

Figure 6 diagrams a problem involving compressive uniaxial loading applied to a rectangular domain in which the load ramps from zero to a sustained value of $\sigma_0 = 2.5$MPa over 10 microseconds. The domain dimensions are $W = 0.08$ m and $H = 0.16$ m. The material properties are: Young's modulus $E = 65$ GPa, mass density $\rho = 2600$ kg/m^3, and Poisson's ratio $\nu = 0.27$. The friction coefficient is $k = 0.3$, corresponding to $\phi = 16.9°$ in the Mohr–Coulomb (MC) effective stress model.

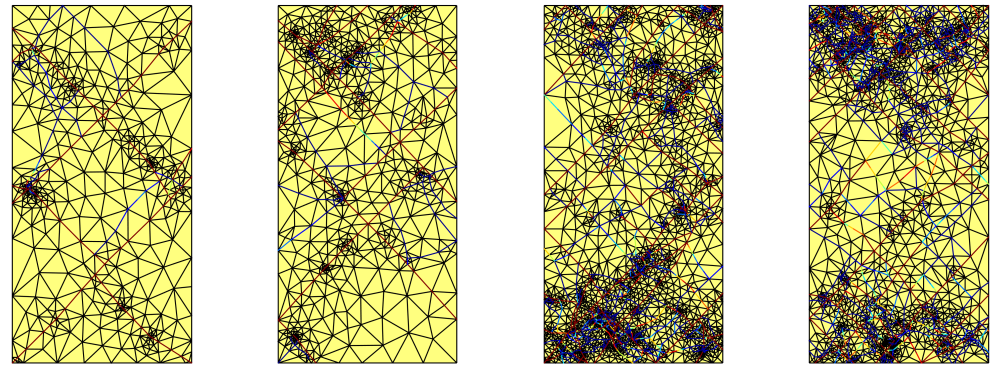

(a) ℓ^2, $A_0 = 1$. (b) ℓ^2, $A_0 = 0.1$. (c) ℓ^2, $A_0 = 0.01$. (d) ℓ^2, $A_0 = 0.001$.

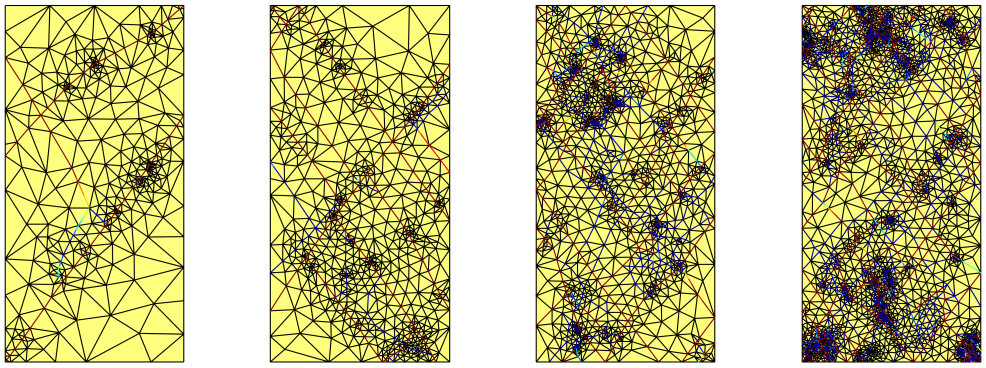

(e) MC, $A_0 = 1$. (f) MC, $A_0 = 0.1$. (g) MC, $A_0 = 0.01$. (h) MC, $A_0 = 0.001$.

Figure 7: Comparison of space meshes and damage for the ℓ^2 and MC effective stress models with varying reference area, A_0. Damage values on crack segments in the range, $D \in [0, 1]$, are mapped to a blue-to-red color range. The solutions are shown for time $t = 150$ μs.

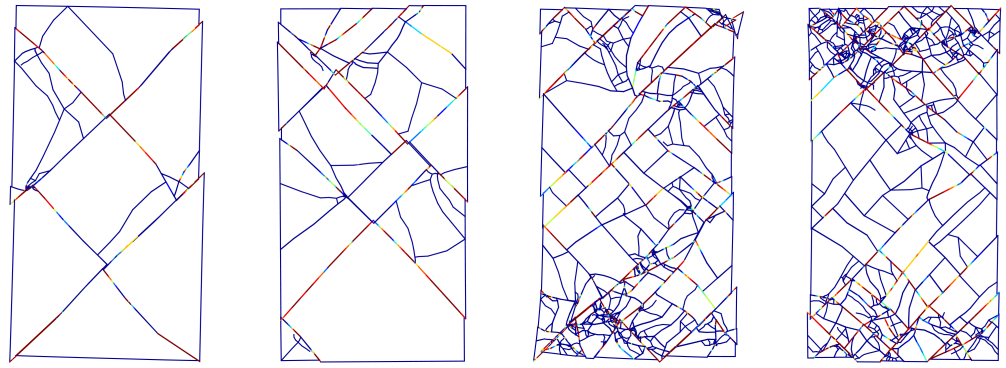

(a) ℓ^2, $A_0 = 1$. (b) ℓ^2, $A_0 = 0.1$. (c) ℓ^2, $A_0 = 0.01$. (d) ℓ^2, $A_0 = 0.001$.

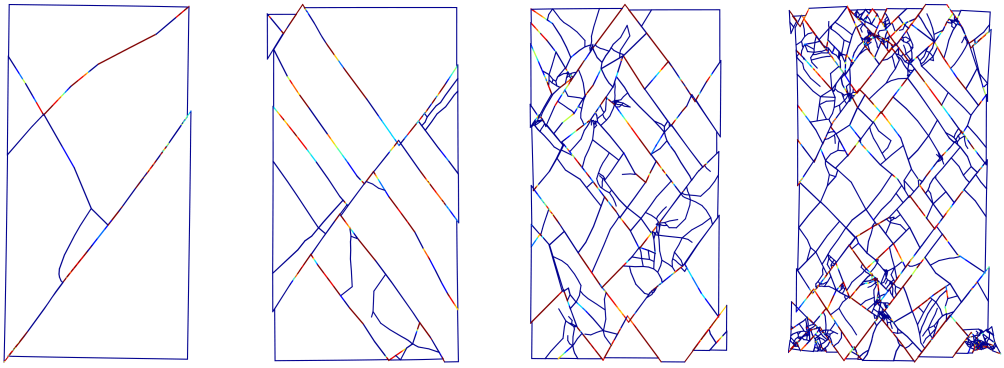

(e) MC, $A_0 = 1$. (f) MC, $A_0 = 0.1$. (g) MC, $A_0 = 0.01$. (h) MC, $A_0 = 0.001$.

Figure 8: Comparison of absolute slip fractions, a_{SL}, for the ℓ^2 and MC effective stress models with varying reference area, A_0. Slip fractions on crack segments in the range, $a_{\mathrm{SL}} \in [0, 1]$, are mapped to a blue-to-red color range. The solutions are shown for time $t = 150$ μs.

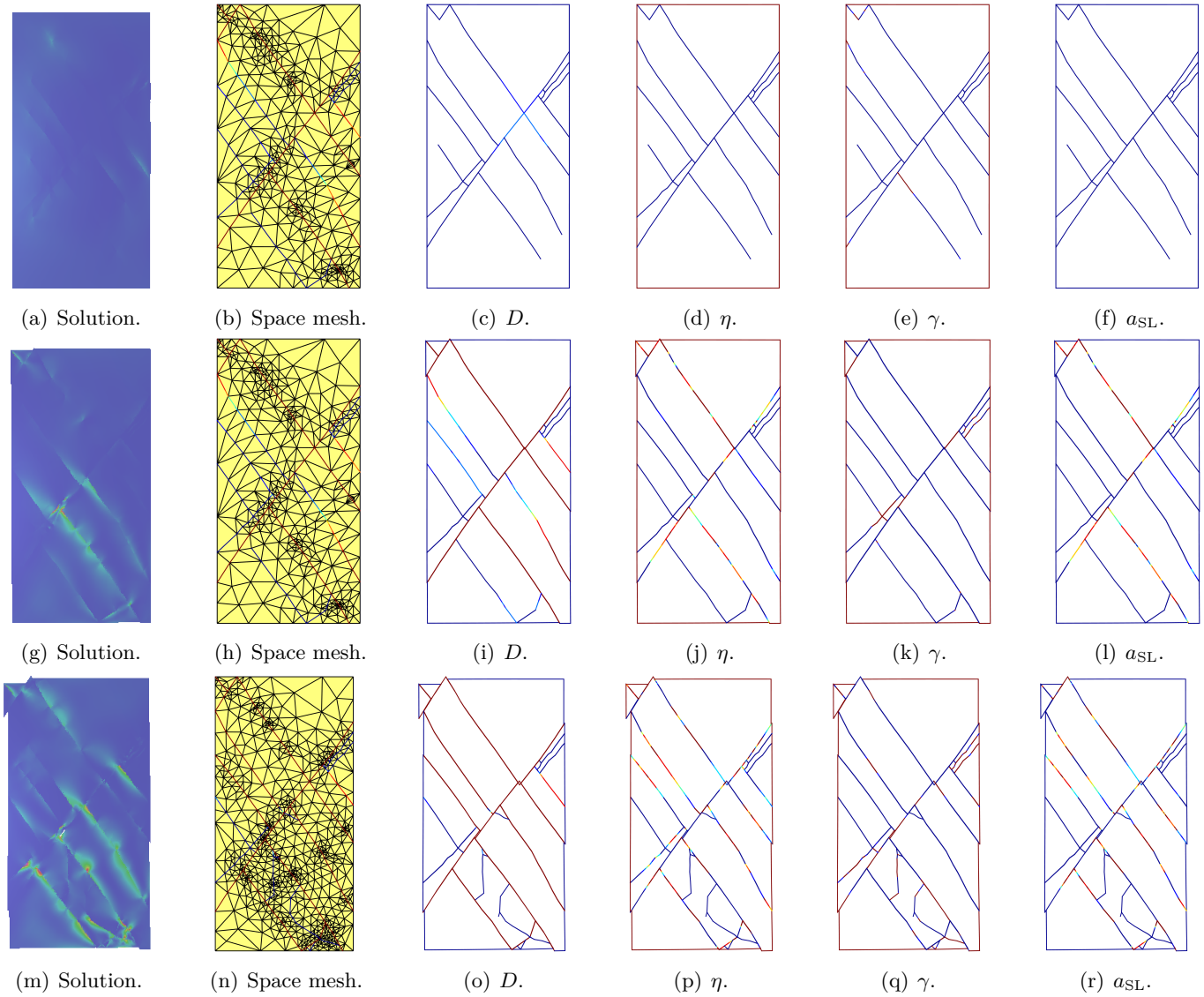

(a) Solution. (b) Space mesh. (c) D. (d) η. (e) γ. (f) a_{SL}.

(g) Solution. (h) Space mesh. (i) D. (j) η. (k) γ. (l) a_{SL}.

(m) Solution. (n) Space mesh. (o) D. (p) η. (q) γ. (r) a_{SL}.

Figure 9: Solution for Mohr–Coulomb effective stress model and reference area, $A_0 = 0.1$. Top, middle, and bottom rows correspond, respectively, to $t = 48\mu$s, 108μs, and 150μs. Color in the solution visualizations in the first column depicts strain energy density; low–high values map to blue–red.

The purpose of this example is to compare the responses of the ℓ^2 and MC effective stress models and to study the influence of stochastic distributions of fracture strength, $\bar{s}$. Specifically, we specify parameters $m = 4$, $\eta = 4$ MPa, and $s_{\min} = 1.1$MPa in the Weibull model. We investigate four values of A_0, chosen to represent a range of weak to strong fracture strengths, as discussed below.

Figure 7 compares crack patterns and adapted meshes using the ℓ^2 (top row) and Mohr–Coulomb (bottom row) effective stress models for four reference area values, $A_0 = 1\mathrm{m}^2$, $0.1\mathrm{m}^2$, $0.01\mathrm{m}^2$, and $0.001\mathrm{m}^2$. The solutions are shown at time $t = 150$ μs, which is substantially past the time compressive waves from the top boundary impinge on those propagating from the bottom boundary at $t = 14.3$ μs. That is, the compressive stresses propagated from the two boundaries have already integrated and generate compressive stresses larger than those generated by each individual wave. These generate mean fracture strengths, $\mathbb{E}(\bar{s}) = 11.88$ MPa, 7.16 MPa, 4.50 MPa, and 3.02 MPa, respectively, for $A = W \times H = 0.0128$ m^2 in (22). The compressive strengths for $k = 0.3$ are $\bar{p}_{\ell^2} = 0.6\bar{s}$ and $\bar{p}_{\mathrm{MC}} = 0.8064\bar{s}$; *cf.* (20a) and (21a).

Before the compressive waves from the two sides intersect in the center horizontal line, the compress stress experienced is $\sigma_0 = 2.5$MPa. A crack is nucleated if $\sigma_0 \geq \bar{p}$ with $\bar{p}$ being a stochastic value, given that $\bar{s}$ is sampled based on the Weibull model. From the values reported above, it is evident that for the two models and $A_0 = 1$ m$^2, 0.1$ m^2 the mean compressive strength is considerably greater than compressive stress σ_0; thus fewer nucleated points are expected. The sampled compressive strengths decrease and more cracks are expected to nucleate as $A_0 \to 0$. This trend is evident in the results obtained with both models, although more cracks are generated with the ℓ^2 model given its slightly lower compressive strengths.

The two models generate distinct fracture angles, as expected. The numerical results for the ℓ^2 model in figs. 7(a-d) agree with the prediction, $\theta_{\ell^2} = 45°$, from (20b).

The crack angles for the Mohr–Coulomb model in figs. 7(e-h) cluster around $\theta_{\text{MC}} = 36.65°$ (measured with respect to the vertical direction), as predicted by (21b). From a computational perspective, it is clear that the h-adaptive aSDG method is fully capable of capturing complex fracture patterns, particularly for smaller values of A_0, and exactly aligning element boundaries with crack propagation directions.

Modifying A_0 to vary the stochastic fracture strength impacts the fracture response in several ways. In fig. 7, we observe more crack nucleations as A_0 decreases, but also, more crack segments with incomplete damage. The increase in nucleations is expected because reducing A_0 reduces the mean nucleation strength. However, a larger fraction of the nucleated cracks fail to reach full damage because higher crack densities produce more dynamic shielding between cracks, and overall, relax the initial dynamic loading. This leads to slower damage rates and more cases of incomplete fracture than in specimens with higher nucleation resistance and fewer cracks.

Figure 8 depicts the absolute slip area fraction $a_{\text{SL}}(10\text{b})$ on crack surfaces in the deformed geometry. This figure confirms that as more cracks nucleate, a smaller fraction of the total fracture surface fully debonds to allow active sliding ($a_{\text{SL}} = 1$). For larger values of A_0, we observe longer fracture segments and longer segments involved in active sliding. Figure 9 depicts various aspects of the evolution of the numerical solution of the Mohr–Coulomb model with $A_0 = 0.1$ to shed more light on the formation and activation of slip lines.

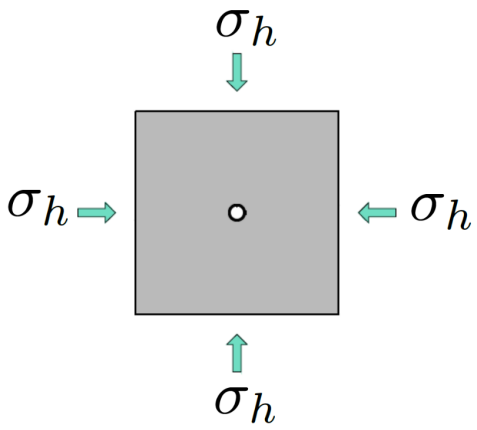

Figure 10: Problem sketch for explosive fracturing example.

5.3 Explosive fracturing

Consider a pressurized wellbore subjected to far-field confining stresses, as shown in Figure 10. The wellbore has a diameter of 30 cm and is subjected to hydrostatic *in-situ* confining stresses, given by $\sigma_h = 2.425$ MPa. The bulk material properties are: Young's modulus $E = 20$GPa, mass density $\rho = 2500$ kg/m^3, and Poisson's ratio $v = 0.2$. The Weibull parameters are $m = 4$, $\eta = 4$MPa, $s_{\min} = 500$kPa, and $A_0 = 0.1$ m^2. An explosive compressive load acts on the wellbore walls, ramping from ambient pressure to 27.5 MPa in 750 ns. Unlike typical hydraulic fracturing practice, there are no pre-cut perforations to initiate fracture in this example. Instead, we rely on the stochastic model of in-situ defects to nucleate fracture.

Figure 11 shows a solution sequence obtained with the Mohr–Coulomb effective stress model. Physically, the high pressures of the detonation cause the rock to fail and compact. After the stress wave passes, the rock unloads elastically, leaving an enlarged, deformed wellbore, a zone of compacted rock and a region of greater compressive stress. The cracks are almost all in shear/compressive mode. Figures 12, 13, 14, and 15 compare solutions, crack patterns, space meshes, and various fields on the crack surfaces from the two effective stress models. The results confirm the enlarged deformed shape and almost instantaneous and uniform damage state around the wellbore. Moreover, figs. 12, 14, and 15 confirm full damage, contact mode, and slip of crack surfaces in this zone. We also observe that the fracture surfaces have propagated well beyond the region of full damage, however, given the finite time needed for damage evolution, *cf.* (11), and attenuation of the compressive wave, they accumulate very little damage. In comparison to the ℓ^2 model, the Mohr–Coulomb model generates slightly steeper crack angles relative to the wellbore surface and has more spread, although its damage zone is less concentrated.

6 CONCLUSIONS

We proposed two effective stress models for crack nucleation and the evolution of interfacial damage on fracture surfaces. We related the models to Tresca and Mohr-Coulomb failure criteria for rock under compressive loading. Our numerical results for a dynamic rock compaction problem demonstrate that the majority of cracks form along directions predicted by the two models. We used a stochastic strength model to nucleate new fractures cracks. Numerical experiments showed that stochastic representations of weaker materials result in more crack nucleation but a smaller fraction reaching full damage and slip conditions.

While our results demonstrate the ability of the damage model and the h-adaptive aSDG method to model and capture complex fracture response, we do not expect the proposed effective stress models to correctly model fracture in rock under more general loading conditions. The ℓ^2 model does not capture the strengthening of rock under increasing confining pressure, and the linearity of the Mohr–Coulomb model over-estimates tensile strength. This results in nonphysical fracture patterns for predominantly tensile crack propagation. We plan to investigate more advanced failure criteria, *e.g.,* [8,24,25], to formulate more robust effective stress models for dynamic fracture in rock.

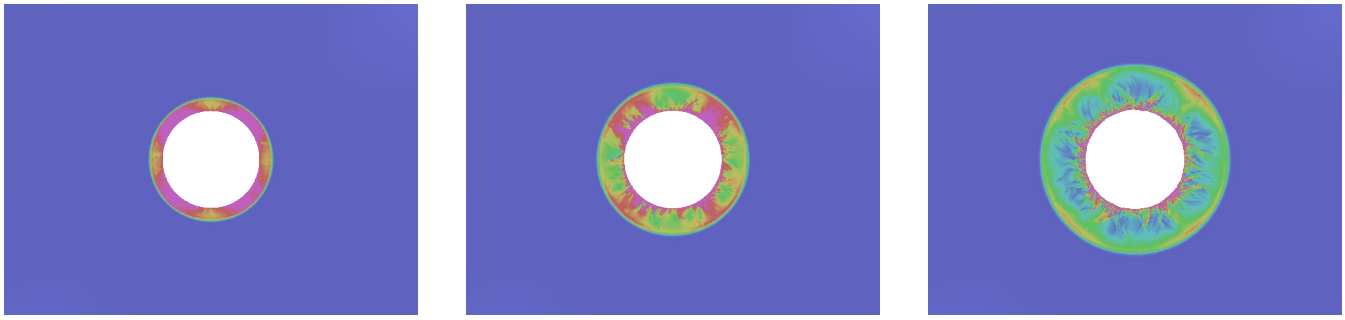

(a) Time $t = 7.5$ μs. (b) Time $t = 15$ μs. (c) Time $t = 25$ μs.

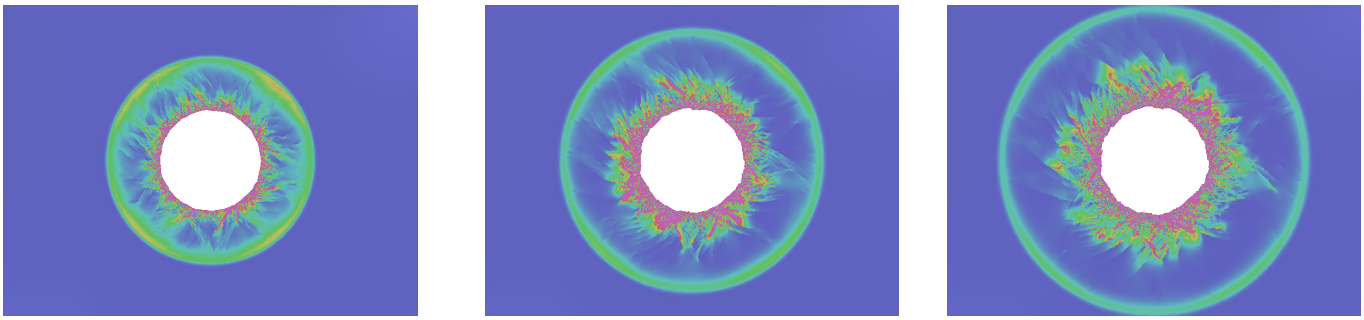

(d) Time $t = 30$ μs. (e) Time $t = 45$ μs. (f) Time $t = 57.5$ μs.

Figure 11: Solution visualization of well fracture with Mohr–Coulomb effective stress model. Strain energy density is mapped to color with blue-to-red range indicating low to high values.

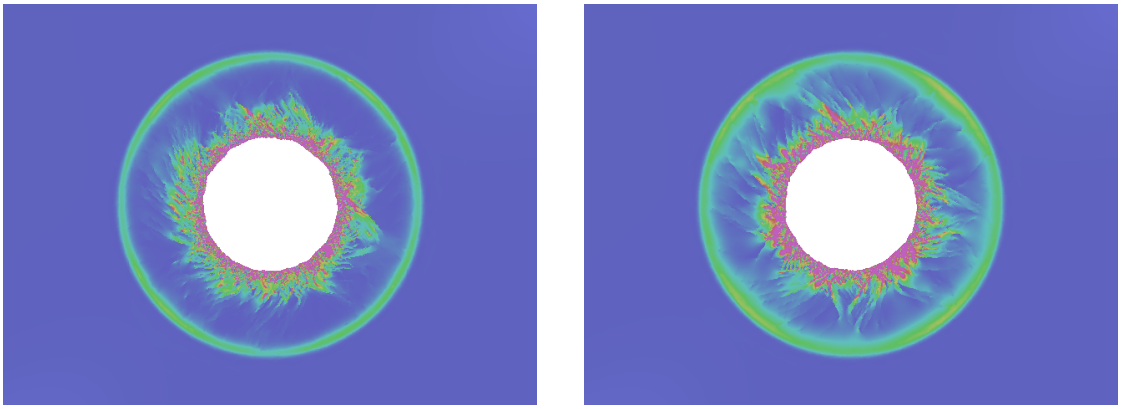

(a) ℓ^2 effective stress model. (b) Mohr–Coulomb effective stress model.

Figure 12: Comparison of solutions for ℓ^2 and MC effective stress models at time $t = 37.5$ μs. Strain energy density is mapped to color with blue-to-red range indicating low to high values.

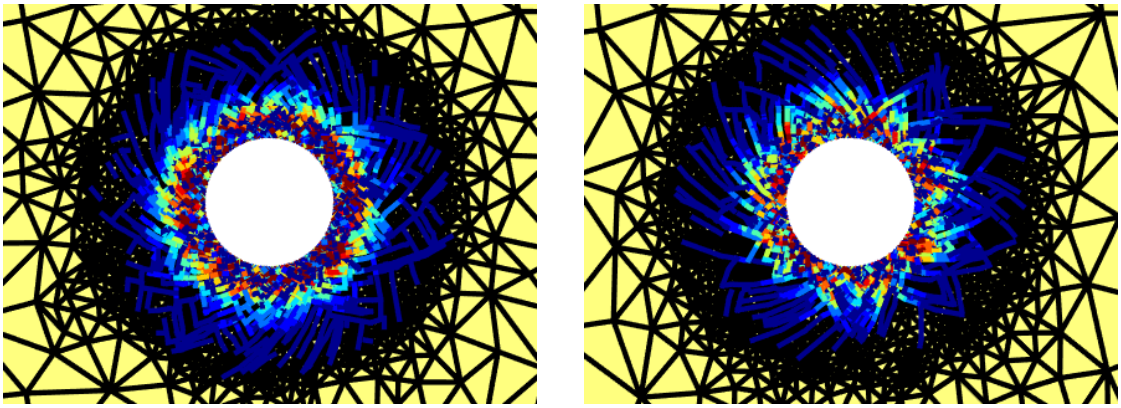

(a) ℓ^2 effective stress model. (b) Mohr–Coulomb effective stress model.

Figure 13: Comparison of space meshes and damage values for ℓ^2 and MC effective stress models at time $t = 37.5$ μs. Damage values on crack segments in the range, $D \in [0, 1]$, are mapped to a blue-to-red color range.

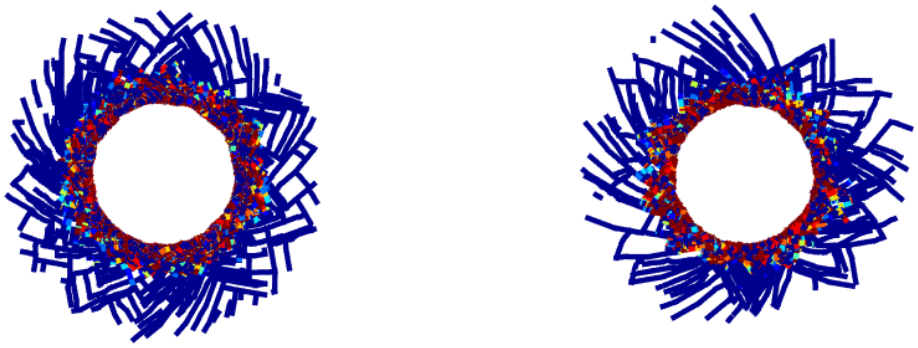

(a) ℓ^2 effective stress model. (b) Mohr–Coulomb effective stress model.

Figure 14: Comparison of crack patterns and contact relative fractions, η, for ℓ^2 and MC effective stress models at time $t = 37.5$ μs. Contact fractions on crack segments in the range, $\eta \in [0, 1]$, are mapped to a blue-to-red color range.

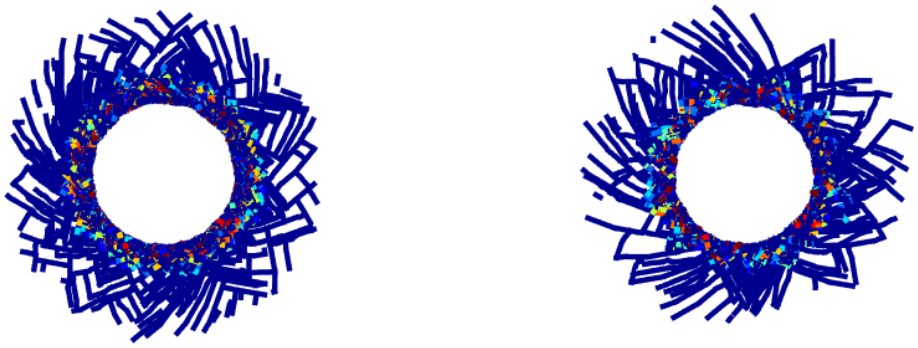

(a) ℓ^2 effective stress model. (b) Mohr–Coulomb effective stress model.

Figure 15: Comparison of crack patterns and contact–slip absolute fractions, a_{SL}, for ℓ^2 and MC effective stress models at time $t = 37.5$ μs. Contact–slip fractions on crack segments in the range, $a_{\mathrm{SL}} \in [0, 1]$, are mapped to a blue-to-red color range.

REFERENCES

[1] Paterson, Mervyn S and Teng-fong Wong (2005) *Experimental rock deformation-the brittle field*. Springer Science & Business Media.

[2] Jaeger, JC and NGW Cook (1979) *Fundamentals of rock mechanics*. Chapman and Hall, New York.

[3] Goodman, Richard E (1989) *Introduction to rock mechanics*, vol. 2. Wiley New York.

[4] Barton, N. and V. Choubey (1977) The shear strength of rock joints in theory and practice. *Rock mechanics*, **10**, 1–54.

[5] Wiebols, GA and NGW Cook (1968) An energy criterion for the strength of rock in polyaxial compression. *International Journal of Rock Mechanics and Mining Sciences & Geomechanics Abstracts*, vol. 5, pp. 529–549, Elsevier.

[6] Zhou, S (1994) A program to model the initial shape and extent of borehole breakout. *Computers & Geosciences*, **20**, 1143–1160.

[7] Ewy, RT et al. (1999) Wellbore-stability predictions by use of a modified lade criterion. *SPE Drilling & Completion*, **14**, 85–91.

[8] Singh, Mahendra, Anil Raj, and Bhawani Singh (2011) Modified mohr–coulomb criterion for non-linear triaxial and polyaxial strength of intact rocks. *International Journal of Rock Mechanics and Mining Sciences*, **48**, 546–555.

[9] Abedi, Reza, Robert B. Haber, and Boris Petracovici (2006) A spacetime discontinuous Galerkin method for elastodynamics with element-level balance of linear momentum. *Computer Methods in Applied Mechanics and Engineering*, **195**, 3247–3273.

[10] Abedi, R., R. B. Haber, S. Thite, and J. Erickson (2006) An h–adaptive spacetime–discontinuous Galerkin method for linearized elastodynamics. *Revue Européenne de Mécanique Numérique (European Journal of Computational Mechanics)*, **15**, 619–642.

[11] Abedi, Reza (2010) *Spacetime damage-based cohesive model for elastodynamic fracture with dynamic contact*. Ph.D. thesis, Department of Theoretical and

Applied Mechanics, University of Illinois at Urbana–Champaign.

[12] Omidi, Omid, Reza Abedi, and Saeid Enayatpour (2016) Well stimulation in tight formations: a dynamic approach. *Proceeding: 50th US Rock Mechanics/Geomechanics Symposium, June 26-June 29, Houston, Texas - USA*, pp. ARMA 16–0150 (12 pages).

[13] Abedi, R., O. Omidi, and P.L. Clarke (2016) Numerical simulation of rock dynamic fracturing and failure including microscale material randomness. *Proceeding: 50th US Rock Mechanics/Geomechanics Symposium, June 26-June 29, Houston, Texas - USA*, pp. ARMA 16–0531 (13 pages).

[14] Abedi, Reza and Robert B. Haber (2014) Riemann solutions and spacetime discontinuous Galerkin method for linear elastodynamic contact. *Computer Methods in Applied Mechanics and Engineering*, **270**, 150 – 177.

[15] Bazant, Zdenek P., Ted B. Belytschko, and Ta-Peng Chang (1984) Continuum theory for strain-softening. *Journal of Engineering Mechanics*, **110**, 1666–1692.

[16] Allix, O., P. Feissel, and P. Thevenet (2003) A delay damage mesomodel of laminates under dynamic loading: basic aspects and identification issues. *Computers and Structures*, **81**, 1177–1191.

[17] Needleman, A. (1988) Material rate dependence and mesh sensitivity in localization problems. *Computer Methods in Applied Mechanics and Engineering*, **67**, 69–85.

[18] Corigliano, A and M Ricci (2001) Rate-dependent interface models: formulation and numerical applications. *International Journal of Solids and Structures*, **38**, 547–576.

[19] Allix, O. and A. Corigliano (1996) Modeling and simulation of crack propagation in mixed modes interlaminar fracture. *International Journal of Fracture*, **77**, 111–140.

[20] Camacho, G. T. and M. Ortiz (1996) Computational modelling of impact damage in brittle materials. *International Journal of Solids and Structures*, **33**, 2899–2938.

[21] Weibull, W. (1939) A statistical theory of the strength of materials. *R. Swed. Inst. Eng. Res.*, p. Res. 151.

[22] Weibull, W. (1951) A statistical distribution function of wide applicability. *Journal of Applied Mechanics*, **18**, 293–297.

[23] Omidi, Omid, Reza Abedi, and Saeid Enayatpour (2015) An adaptive meshing approach to capture hydraulic fracturing. *The 49th US Rock Mechanics/Geomechanics Symposium, June 28-July 1, San Francisco,CA,USA*.

[24] Hoek, E. and T. Brown (1980) *Underground Excavations in Rock*. Geotechnics and foundations, Taylor & Francis.

[25] Hoek, E, CT Carranza-Torres, and B Corkum (2002) Hoek-brown failure criterion–2002 edition. *In Proceedings of Proceedings of the fifth North American rock mechanics symposium*, Toronto, Canada, vol. 1, pp. 267–273.